**SANDIA REPORT**
SAND2019-1030
Printed Click to enter a date

# A platform for quantum information and large-scale entanglement with Rydberg atoms in programmable optical potentials

Michael J. Martin, Melissa C. Revelle, and Grant W. Biedermann

Prepared by
Sandia National Laboratories
Albuquerque, New Mexico
87185 and Livermore,
California 94550

Issued by Sandia National Laboratories, operated for the United States Department of Energy by National Technology & Engineering Solutions of Sandia, LLC.

Available to DOE and DOE contractors from
U.S. Department of Energy
Office of Scientific and Technical Information
P.O. Box 62
Oak Ridge, TN 37831

| | |
|---|---|
| Telephone: | (865) 576-8401 |
| Facsimile: | (865) 576-5728 |
| E-Mail: | reports@osti.gov |
| Online ordering: | http://www.osti.gov/scitech |

Available to the public from
U.S. Department of Commerce
National Technical Information Service
5301 Shawnee Rd
Alexandria, VA 22312

| | |
|---|---|
| Telephone: | (800) 553-6847 |
| Facsimile: | (703) 605-6900 |
| E-Mail: | orders@ntis.gov |
| Online order: | https://classic.ntis.gov/help/order-methods/ |

# ABSTRACT

Large-scale quantum systems with controllable interactions are important for understanding complex phenomena in nature, and are the basis for advanced quantum technologies. Realizing a controllable platform for controlling, understanding, and ultimately harnessing the entanglement is an outstanding challenge in quantum science. This project demonstrated reconfigurable arrays of individually-trapped ultracold atoms, thus realizing a platform that could demonstrate large-scale quantum entanglement with the addition of strong inter-atomic interactions. Arrays of more than 50 trap sites were formed via digital holography and a high-numerical aperture imaging system that featured in-situ trap diagnostics and single-atom imaging resolution. We further discovered a new implementation of a controlled-phase gate that utilized coherent excitation to Rydberg states. This method will enable robust entanglement protocols in many-atom systems such as the one developed here.

# ACKNOWLEDGEMENTS

We would like to acknowledge support from the Sandia National Laboratories LDRD program.

## CONTENTS

## LIST OF FIGURES

This page left blank

# ACRONYMS AND DEFINITIONS

| Abbreviation | Definition |
|---|---|
| AI | analog in |
| AO | analog out |
| AOM | acousto-optic modulator |
| AR | anti-reflection |
| CCD | charge-coupled device |
| DDS | direct digital synthesizer |
| DIO | digital input/output |
| EMCCD | electron multiplying charge-coupled device |
| FM | frequency modulation |
| FPGA | field-programmable gate array |
| GPU | graphics processing unit |
| ITO | indium tin oxide |
| MOT | magneto-optical trap |
| NA | numerical aperture |
| PM | polarization maintaining |
| SLM | spatial light modulator |
| SPI | serial peripheral interface |
| UV | ultra-violet |

# 1. INTRODUCTION

Strongly-interacting quantum systems are a central theme of modern physics. Nature provides a large range of systems for which quantum effects play a dominant role, such as high-Tc superconductors and quantum magnetic materials. Notably, some of the complex quantum behavior in these systems has eluded scientists, despite decades of focused work. An alternative approach to understanding complex quantum systems is to build them from the ground up, with control over interactions and geometry. Such an approach allows studies of complex quantum systems over a tunable parameter space, which can yield insights into quantum systems whose behavior is poorly-understood. Furthermore, control over the size, interactions and geometry of a quantum system can provide new tools for quantum measurement, including highly entangled systems for sensing [1] and control techniques for optimal control in the presence of noise [2].

Because of the promise of controlled quantum many-body systems, developing the fundamental building blocks has been pursued on a variety of platforms, including trapped ions, polar molecules, and neutral atoms [3, 4, 5, 6, 7, 8, 9, 10, 11, 12]. Of these approaches, neutral atoms offer rapid scalability [10, 13, 14] and a heritage of ultra-precise quantum sensing [15]. Examples of neutral atom quantum systems include quantum gases of fermions or bosons in optical lattices [16], and individual atoms in optical tweezers [17, 18], the approach taken here.

The quantum gas approach uses itinerant particles (particle that are free to hop between lattice sites via quantum tunneling), where the interplay of tunneling and interactions yields rich behavior that can mimic electrons in condensed matter systems [16, 19]. By cooling Fermions or Bosons deep into quantum degeneracy, one enters a regime where tunneling and inter-particle interactions dominate the behavior of the system, realizing the paradigm of a quantum phase transition [20]. In multi-component quantum gas systems, super-exchange interactions can mimic important effects found in highly-correlated electronic material, where the spin-dependent interaction of electrons plays a central role in the material properties. Because the interaction energy in this approach scales as $t^2/U$, where $U$ is the interaction energy of a dual-occupancy lattice site, and $t$ is the tunneling rate, the wavelength of light and particle mass sets limits on the energy scale of interactions based on the super-exchange mechanism [21, 22]. The temperature scales required to reach predicted quantum phase transitions in this approach is challenging to reach experimentally, although recently antiferromagnetic ordering has been observed in a fermionic Lithium quantum gas microscope system [19]. These types of systems are very powerful for studying the Fermi-Hubbard model, which can describe the quantum dynamics of highly-correlated condensed matter systems, at a range of electron doping.

A different paradigm for an interacting quantum system is found in systems that effectively freeze the constituent particles in place, but rely on long-range, spin dependent interactions to create entanglement. Examples of this latter type of system include ultracold polar molecules [23], trapped ions [24], and Rydberg atoms [25]. While these systems are not comprised of itinerant particles, they still constitute powerful quantum systems, with interaction energy scales many orders of magnitude, leading to quantum entanglement at much shorter timescales. Instead of relying on super-exchange to realize spin-dependent interactions, these systems utilize couplings that arise from Coulomb, dipolar, or strong van der Walls interactions. Most notably, in this type of approach the details of system geometry and interaction strength are tunable via external control parameters, such as applied fields, and laser tuning. Compared to the itinerant atom approach, these systems are far more robust to thermal fluctuations, and are more broadly tunable, and thus provide a

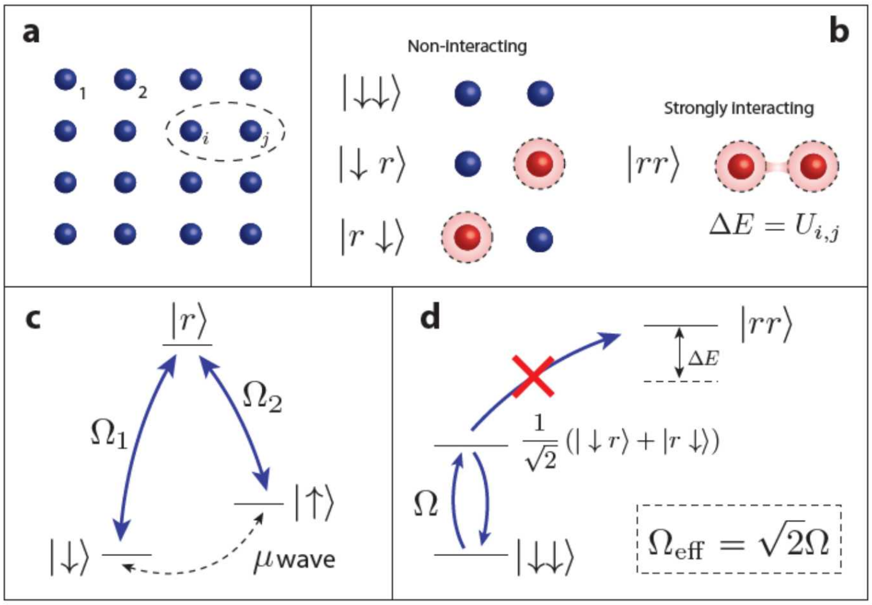

**Figure 1** Interactions between Rydberg atoms can lead to entangled states. (a) A pair of atoms can be excited (b) to rydberg levels with large energy shift for pair state with both atoms in the Rydberg state. (c) Ground state levels can be coupled to the Rydberg manifold. (d) When the energy shift of the double-excited Rydberg state is greater than the Rabi frequecy $\Omega$ , the system evolves into and out of the entangled Bell state with effective Rabi frequency $\sqrt{2}\Omega$.

complimentary approach to studying complex quantum matter, such as frustrated quantum magnetism [22], and provide a platform for developing quantum technologies that leverage the control over interactions and entanglement [1].

Of these latter technologies, the strongest typical interaction scales come from Rydberg atoms, which possess several desirable characteristics, and were recognized almost two decades ago to be a promising system for quantum information [21]. The utility and flexibility of Rydberg atoms arises from the fact that they can be selectively and deterministically excited to strongly-interacting Rydberg states. Specifically, Rydberg atoms are atoms where a single valence electron occupies a very high principle number orbital, $n$ , where $n$ can be greater than 100. Rydberg atoms possess a greatly enhanced van-der-Waals interaction that scale as $n^{11}$ and as $r^{-6}$ with atomic separation (see, e.g., Ref. [22] for a review of the properties of Rydberg atoms). For example, the interaction energy[1] of two Rydberg atoms separated by $10\ \mu\text{m}$ can be of order $h \times 10$ MHz , where $h$ is Planck's constant. As a result, entangling operations between atoms, such as the one shown in Figure 1, can occur on the microsecond time scale. Because of the strong dependence of the interaction strength on interatomic separation, the interatomic spacing can set the scale of relevance for the interactions. Thus, highly controlled, large-scale, and strongly interacting systems are possible with ensembles of Rydberg atoms.

In a many-body systems, the Rydberg interaction energy can be expressed as a pairwise interaction term, such that the Hamiltonian for the system becomes

---

[1] Please note that energy and frequency are used interchangeably throughout this report. Any reference to energy in units of frequency will implicitly include a conversion factor of Planck's constant.

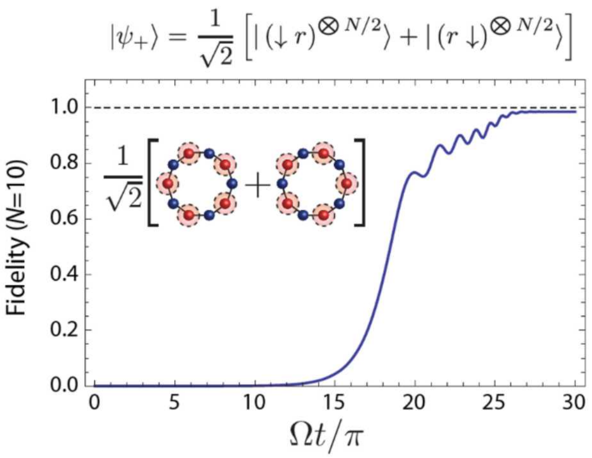

**Figure 2** By dynamically sweeping Rabi frequency and detuning, highly-entangled states can be adiabatically prepared. Here, the preparation fidelity of a superposition state of crystalline phases is calculated. The energy cost of adding an additional Rydberg excitation facilitates rapid adiabatic passage to this ordered state. By flipping the state of every other atom, this superposition state can be converted to a GHZ state.

$$\hat{H} = -\Delta\sum_i |r_i\rangle\langle r_i| + \sum_{i<j} U_{ij}\,|r_i r_j\rangle\langle r_i r_j| + \frac{\Omega}{2}\sum_i |g_i\rangle\langle r_i| + |r_i\rangle\langle g_i|\ , \tag{1}$$

where $\Delta$ is the laser detuning from the ground state to Rydberg state transition, $\Omega$ is the Rabi frequency that describes the atom-light coupling and $U_{ij}$ is the pairwise van der Waals interaction between Rydberg atoms, with characteristic $1/r^6$ dependence. The coupling to the Rydberg state can be a single-photon [23] or multi-photon process [11, 12]. By dynamically controlling $\Omega$ and $\Delta$, many-body phase transitions can be probed [24], crystallized states emerge [25] and highly-entangled states can be prepared [26]. Figure 2 shows the preparation of such an entangled state via adiabatic sweep, which can be converted to a GHZ state via individual addressing of atoms. Generally speaking, interactions of the type described in Equation (1) can map onto Ising models that describe quantum magnetism [27].

Optical dipole trapping of neutral atoms has become a standard technique in atomic physics [28]. For a spatially-dependent optical field with intensity $I(\mathbf{r})$, the spatially-dependent optical potential is given by

$$U(\mathbf{r}) = \frac{-\alpha(\omega)}{2\varepsilon_0 c} I(\mathbf{r})\ . \tag{2}$$

In the case of a Gaussian beam profile, the potential takes the form [29]

$$U(r,z) = U_0 \frac{e^{-2r^2/w(z)^2}}{1+(z/z_R)^2}\ , \tag{3}$$

with $z_R = \pi w_0^2/\lambda$, and corresponding trap frequencies given by $\omega_r = \sqrt{\frac{4U_0}{m w_0^2}}$ and $\omega_z = \sqrt{\frac{2U_0}{m z_R^2}}$ for the radial and longitudinal directions.

To enter the optical tweezer regime requires a sufficiently tight focus such that there is strong three-dimensional confinement, meaning the trap oscillation frequencies are comparable in

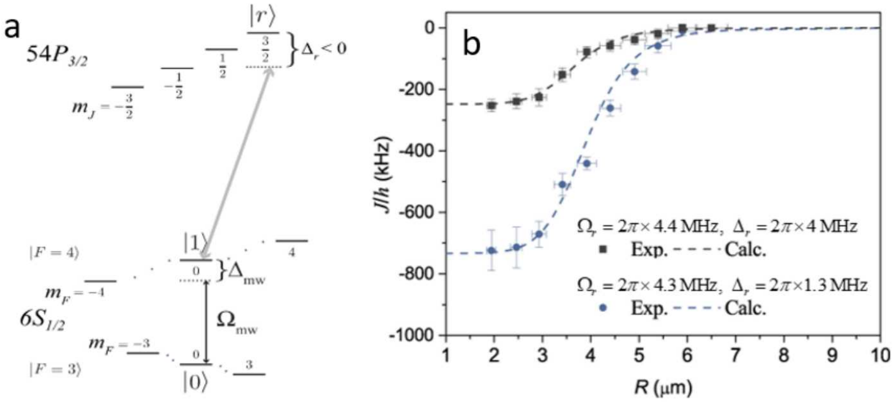

**Figure 3** (a) The ground state qubit levels and the Rydberg level form an effective 3-level system. By admixing the qubit state $|1\rangle$ with the Rydberg state via laser dressing, the three level system maps back to a two level-system with strong interactions between the dressed gound states $|\tilde{1}\rangle$. (b) The Rydberg dressing process leads to a tunable interaction between atoms with a soft-core character. Plots adapted from Ref. [33].

radial and longitudinal directions, which occurs when $w_0 \simeq \lambda$. Entering into this regime requires high numerical aperture (NA) lenses, as focal spot diameter scales as $d_f = \chi\lambda / \text{N.A.}$, where $\chi$ is a constant of order unity. For uniform illumination, $\chi \simeq 1.22$. This is the well-known Rayleigh criterion, where $d_f$ represents the diameter of the first minimum of the Airy disc. In the case of Gaussian illumination, for the case where $w0$ matches the input aperture radius, $\chi = 2/\pi$ and $d_f$ represents the $1/e^2$ intensity diameter of the resulting pattern in the focal plane.

Typical values of $U_0$ in units of the Boltzmann constant $k_B$ are in the 1 mK range, as this is at least an order of magnitude deeper than typical temperatures achieved via standard laser cooling techniques. We note that in this optical tweezer regime, the trap volume is sufficiently small such that the trap loading is nonlinear—due to light-assisted collisions—and saturates in the single-atom loading regime [17]. This is an added benefit to the precise control over center of mass that tight confinement enables, because it ensures trap occupancy is either zero or one atoms.

We note that in the time since this project began, there has been a revolution in using optical tweezers to create 1-, 2-, and 3-dimensional structures deterministically [30, 13, 31, 14]. At the basic level, all of these schemes use some form of atom re-arrangement by moving atoms into defect sites where an atom is missing from the desired configuration. The two main strategies are tweezer based "pick and place" operations, one-dimensional "accordion" compactification, or dynamic hologram updates. These authors have demonstrated defect-free arrays of up to 50 atoms.

In addition to the interaction between two Rydberg levels, another approach utilizes optical fields to dress a metastable ground state [32, 33, 34], such that it acquires some of the interacting character of Rydberg state. The Rydberg-dressed interaction creates an admixture of a ground state atom with long coherence time and a Rydberg state atom. By tuning this admixture with a well-controlled coupling laser, the strength of the interaction can be controlled dynamically during the experiment. For the case of ground state hyperfine qubits $|0\rangle = |F = 3, m_F = 0\rangle$ and $|1\rangle = |F = 4, m_F = 0\rangle$, dressing creates a superposition $|1\rangle \to |\tilde{1}\rangle = \alpha|1\rangle + \beta|r\rangle$ when connected to the Rydberg state via a single photon as shown in Figure 3a. In analogy to the Rydberg interaction between two excited atoms, the interaction between dressed atoms takes the form

$$\hat{H}_{DD} = J\,|\tilde{1}\tilde{1}\rangle\langle\tilde{1}\tilde{1}| \tag{4}$$

where the interaction strength $J$ takes the form of a soft-core potential, shown in Figure 3b. In the limit of strong blockade where $U_{rr} \gg \Omega$, $J$ becomes independent of separation, and is given by

$$J = \frac{\Delta_r + \sqrt{2\Omega_r^2 + \Delta_r^2}}{2} - \sqrt{\Omega_r^2 + \Delta_r^2}\ . \tag{5}$$

Via dressing, the blockade can occur directly through microwave excitation of the qubits. The process is similar to the direct excitation approach, although has several advantages, including tunable interaction, reduced light shifts, and nonlinear multibody interactions with connections to the Jaynes-Cummings model of cavity QED [2].

# 2. PRELIMINARY WORK

A key pre-requisite for any many-body system is the capability to drive the system coherently and that the many-body interaction is well-controlled and coherent. A two-atom experiment is the ideal test-bed to verify these pre-requisites. In this section, we describe work on a two-atom Rydberg experiment that supports the scientific goals of this project.

## 2.1. Two-atom Rydberg experiment

The experiment is described in detail in [29, 33, 35], but we describe the relevant details here. As shown in Figure 4, two atoms are trapped in optical tweezers that are approximately 100 $\mu$K to 1 mK deep, with atoms that are cooled via polarization-gradient cooling and adiabatic ramping to reach temperatures $\leq 10\ \mu$K in a 100 $\mu$K deep trap. The inter-atomic spacing is controlled via acousto-optic deflection. The internal state of the atom is measured via fluorescence measurement via fiber-coupled single photon counting modules. Microwave control of the two ground qubit states, $|1\rangle = |F=4, m_F=0\rangle$ and $|0\rangle = |F=3, m_F=0\rangle$, is achieved via a two-photon Raman transition detuned approximately 80 GHz from the Cs D2 transition. Extensive shielding and eight electrode pairs provide shielding against and control of electric fields.

As described in Section 1, a crucial technological innovation of this system was the development of an ultraviolet (UV) laser to directly excite Cesium atoms in the $5S_{1/2}$ ground state to the $nP$ Rydberg manifold [36]. This direct excitation approach offers advantages over two-photon schemes for exciting Rydberg states, namely there is no intermediate state to cause decoherence, and that the direct approach facilitates laser dressing of one of the qubit states [33].

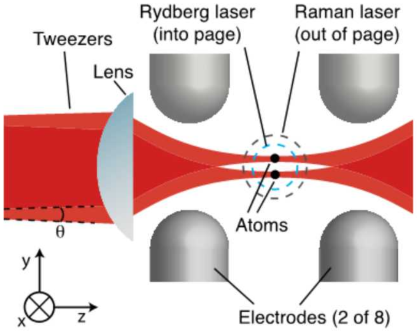

**Figure 4** Schematic of the two-atom experiment. Two atoms are trapped in tweezers in a controlled environment. An ultraviolet laser (into page) couples the $|F=4, m_F=0\rangle$ ground state to the Rydberg level.

## 2.2. Coherence of Rydberg blockade

A prerequisite for building a complex quantum system is that at the single- and few-atom level, the behavior is coherent, with minimal dephasing and noise. In order to explore whether the many-atom systems could demonstrate the necessary coherence to achieve the goals of this project, we first explored the two-atom coherence properties under direct excitation to the Ryberg state. The Hamiltonian that describes this experiment is

$$\hat{H} = -\Delta \sum_i |r_i\rangle\langle r_i| + \sum_{i<j} U_{ij} |r_i r_j\rangle\langle r_i r_j| + \frac{\Omega}{2} \sum_i |g_i\rangle\langle r_i| + |r_i\rangle\langle g_i|. \tag{6}$$

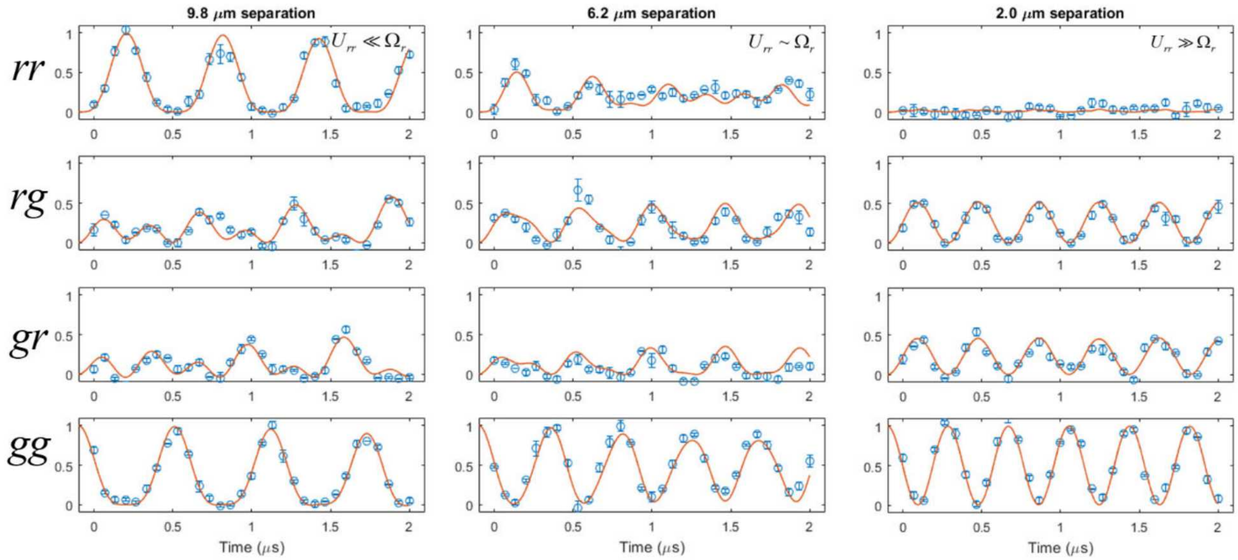

**Figure 5** Resonant excitation of the $54\mathrm{P}_{3/2}$ level of a pair of atoms at varying separation. At the largest separation (left), the blockade is weak, and the Rydberg interaction only weakly affects the system evolution. At intermediate separation the interaction strongly affects the dynamics. At closest separation, the doubly-excited state is completely blockaded, and the system maps onto an effective two-level system.

Here, $\Delta$ is the laser detuning from the ground state to Rydberg state transition, $\Omega$ is the Rabi frequency that describes the atom-light coupling and $U_{ij}$ is the pairwise van der Waals interaction between Rydberg atoms, with characteristic $1/r^6$ dependence. In the case of two atoms, $i$ and $j$ take the values 1 or 2, and the interaction part of the hamiltonian is particularly simple, reducing to a single term $\hat{H}_{\text{int}} = U_{rr} \, |r_1 r_2\rangle\langle r_1 r_2|$.

As shown in Figure 5, we explore three different parameter regimes. Starting with the atoms in the $|g\rangle = |F=4, m_F=0\rangle$ state, we directly excited the Rydberg transition with light resonant to the Rydberg transition for varying atom separations $r \in \{9.8, 6.2, 2.0\}\ \mu\text{m}$. The experiment proceeds by dropping both atoms, illuminating with the UV Ryberg laser for a given duration of time, then detecting the presence or absence of atoms in each tweezer once the optical tweezer beams are turned back on. It is assumed that loss events are due to excitation to the Rydberg manifold, and thus other loss events must be accounted for. Across the three parameter regimes of Figure 5, with Rydberg interaction strength less than, comparable to, and greater than the Rabi frequency, three qualitatively different regimes are observed. Notably, the dynamics of this system are well-described by coherent evolution of Equation (6), with minor corrections to include slightly different Rabi frequencies between the two atoms. Specifically, in the strongly-interacting regime $U_{rr} \gg \Omega$, we see that excitation to the doubly excited Rydberg state is completely blockaded, and the population oscillations in the doubly occupied ground state have a shorter period. This is indicative of a complete Rydberg blockade, where the system is reduced to an effective two-level system between the $|gg\rangle$ and $\left(|gr\rangle + |rg\rangle\right)/\sqrt{2}$ states, the latter of which is a maximally entangled two-atom state known as a Bell state. It is also important to note that we corrected for the effect of

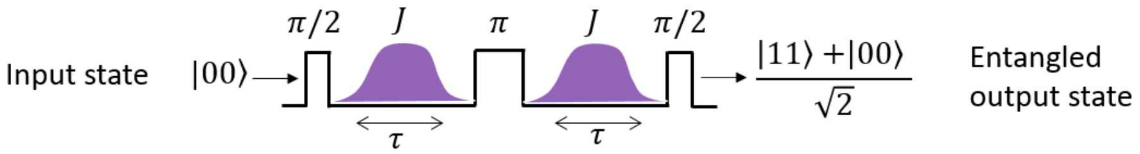

**Figure 6** Pulse sequence for the CPHASE protocol. The spin echo topology removes single-atom light shift terms, yielding an effective interaction Hamiltonian of the form $\exp\left\{-i\phi_J \hat{S}_z^2\right\}$.

loss by using detection errors as a fitting parameter. The inferred errors in loss-based detection rates agree with other measurement methods.

We conclude that the quantum dynamics of the two atom system driven from $|g\rangle \rightarrow |r\rangle$ with the UV Rydberg laser are coherent to our level of resolution. This result demonstrates that the dynamics described by Equation (6) should scale to larger systems, and this has been explored in experiments using two-photon transitions to the Rydberg state [24, 37, 38]. Single photon dynamics, like those shown here, should therefore allow for highly coherent studies of Ising physics without the extra decoherence induced by the intermediate state of the two-photon approach.

## 2.3. CPHASE demonstration

In the previous section we described an experiment using direct excitation to probe the strong van der Waals interaction in a system comprising two atoms. A second approach, described in Section 1, is to Rydberg dress one of two metastable ground state qubit states. This endows the dressed ground state with a tunable interaction that can be two- or multi-body in nature [2, 39]. Because the interaction can be tuned with dressing laser parameters, as well as the clear advantage of using ground metastable states as a quantum register, the dressing approach is highly desirable for inducing interactions in a quantum many-body system. Therefore, motivated by these benefits, we also explored using a coherent entangling mechanism that would benefit many-atom systems.

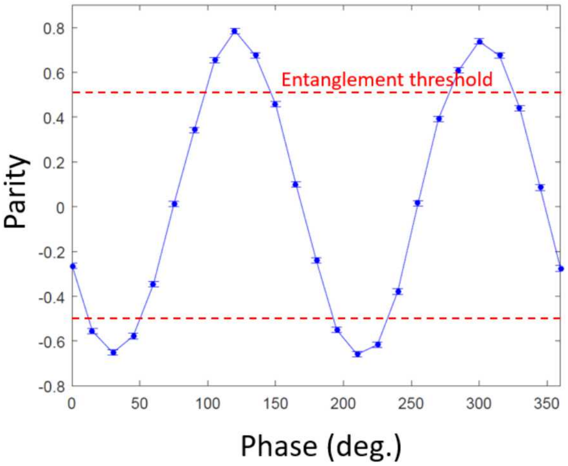

**Figure 7** Parity oscillation after preparing a GHZ state and performing an additional $\pi/2$-pulse with varying phase.

In many-atom systems, it is often desirable to prepare an initial un-entangled state, and then apply an entangling Hamiltonian. This is particularly relevant for Hamiltonians that can induce useful correlations between atoms, such as is the case for spin squeezing [1, 40]. To test this, we set out to perform an entangling operation on an initial state such that

$$|\psi_0\rangle = \frac{1}{4}\left(|00\rangle+|10\rangle+|01\rangle+|11\rangle\right) \rightarrow \frac{1}{4}\left(|00\rangle+|10\rangle+|01\rangle+e^{i\phi_J}\,|11\rangle\right). \qquad (7)$$

To accomplish this, we used the dressing sequence shown in Figure 6, where the addition of the spin echo pulse removed single-atom light shifts from the Rydberg dressing protocol. This sequence yields an effective $\hat{S}_z^2$-type Hamiltonian that acts on the pseudospin-1 space of the two particles. Specifically, the time evolution between the two $\pi/2$ pulses is given by

$$\hat{U}_{\text{echo}} = \hat{U}_1(\tau)\hat{U}_x(\pi)\hat{U}_1(\tau) = \exp\left\{-i\phi_J\hat{S}_z^2\right\}\hat{U}_x(\pi) \tag{8}$$

with $\phi_J = \int_{t_0}^{t_0+\tau} dt' J(t')$, where $J$ is given by Equation (5). When $\phi_J = \pi/2$, the output state for the sequence shown in Figure 6 is a Bell state. We measured the off-diagonal elements of the density matrix of the prepared Bell state using parity measurements [41] and find that the fidelity of the prepared state is >70%. A detailed analysis of this entangling operation was subsequently performed in Ref. [42]. However, this initial demonstration is significant because it shows that entangling operations can be performed an initial superposition of ground states, such as coherent spin states, which greatly enhances the possibilities of many-body systems of neutral atoms for quantum simulation and information, and entanglement-enhanced sensing.

# 3. APPARATUS

In this section we describe the apparatus that we developed for creating reconfigurable arrays of trapped atoms. At the beginning of this work, there had been several demonstrations of trapping atoms in arrays derived from computer-generated holograms [43, 44]. Notably, in the time since this project began, there have been significant advances in the creation of tweezer-based arrays of neutral atoms in one [24], two [13, 45, 30], and three dimensions [14, 46] based on this approach.

## 3.1. Digital Holography

Phase-only spatial light modulators (SLMs) are liquid crystal-based devices (typically liquid crystal on silicon) that can impart a spatially-dependent phase shift to light with both high spatial and phase resolution. For instance, state-of-the-art devices can have over 1 million total pixels, each with 12 bits of phase resolution and pixel sized below 10 microns.

Because of the Fourier transforming properties of lenses in optical systems, a phase mask in the image plane can be converted to a desired intensity pattern with high efficiency. Specifically, as shown in Figure 8, an input field distribution in the object plane, $E_{\text{in}}(\xi,\eta)$, is modified by the SLM phase mask $\mathcal{M}(\xi,\eta)=\exp\left[i\phi_{\text{SLM}}(\xi,\eta)\right]$, such that

$$E_{\text{in}}(\xi,\eta)\rightarrow\exp\left[i\phi_{\text{SLM}}(\xi,\eta)\right]E_{\text{in}}(\xi,\eta)\ . \tag{9}$$

After Fourier transforming by a lens, the output field is related to the input field by [47]

$$E_{\text{out}}(u,v)=\frac{1}{i\lambda f}\mathcal{F}\left[E_{\text{in}}(\xi,\eta)\right]\star\mathcal{F}\left[\mathcal{M}(\xi,\eta)\right]\ , \tag{10}$$

where $\mathcal{F}\left[g(x,y)\right]\equiv\int e^{-i2\pi(xu+vy)}g(x,y)dxdy$, the star represents the convolution operation, and the scaled output coordinates $u,v$ are related to the real space output coordinate by $(u,v)=(x,y)/(\lambda f)$, where $\lambda$ is the wavelength of the illuminating light and $f$ is the lens focal length.

For this project, the desired intensity pattern in the output plane is arrays of diffraction-limited Gaussian beam foci—optical tweezer arrays. Because the input illumination is typically Gaussian, this requires approximating a phase mask such that

$$\mathcal{F}\left[\mathcal{M}(\xi,\eta)\right]=\sum_{i}^{N}e^{i\Delta\phi_i}\delta\left(u-\frac{x_i}{\lambda f},v-\frac{y_i}{\lambda f}\right), \tag{11}$$

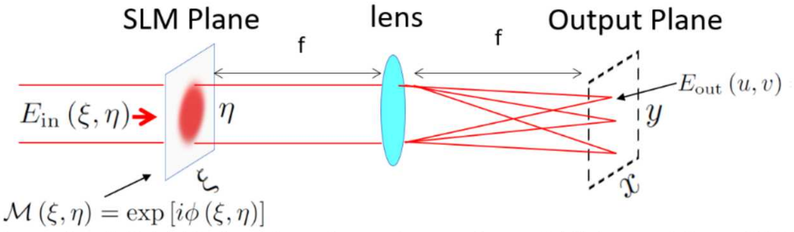

**Figure 8** Simplified schematic of digitial holgraphy using a phase-only spatial light modulator (SLM). The SLM lies in the Fourier plane of the objective lens. The electric field amplitude in the output plane is related to the phase-modulated input by a simple fourier transform.

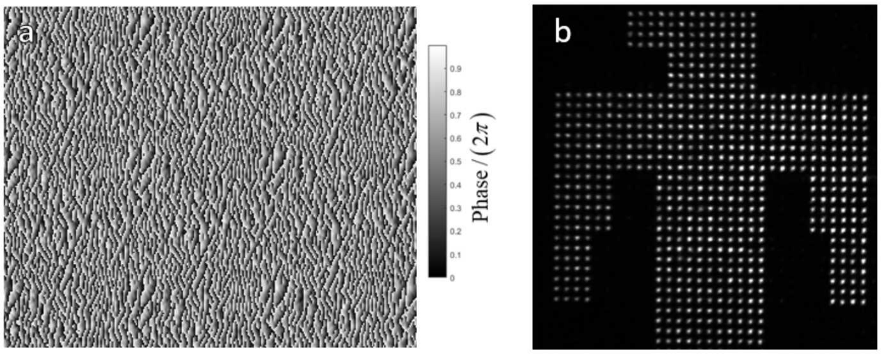

**Figure 9** (a) Example computer-generated hologram and (b) its corresponding image in the Fourier plane.

where $\delta(\ )$ is the Dirac delta function and $\{x_i, y_i\}$ are the locations of the traps. The convolution in Equation (10) will then generate the trap array. Because we only care about trap intensity, not phase, the relative phases of individual traps are free to vary with respect to one another, represented here by $\Delta\phi_i$.

The problem of finding $\phi_{\text{SLM}}(\xi,\eta)$ such that Equation (11) is approximately satisfied can be performed with an iterative Fourier Transform algorithm known as the Gerchberg-Saxton algorithm [48]. We follow the approach of Nogrette *et al.* in implementing this algorithm [44]. Specifically, we use a Gaussian weighted input amplitude and Gaussian target array. For an input amplitude $\propto e^{-(\xi^2+\eta^2)/w_0^2}$, the target array Gaussian amplitude radius is chosen so that it is related to the diffraction-limited spot size corresponding to the input waist, such that $w_0^{\text{target}} = \lambda f / (\pi w_0)$. Including this Gaussian smoothing in the target plane also makes it easier to define the center of mass of the each tweezer in the target plane, compared to a discrete delta function without the Gaussian profile.

Because SLMs can have update rates >100 Hz, we identified early in this project that real-time transport of trapped atoms could be performed if phase holograms could be calculated sufficiently quickly. Because the Gerchberg-Saxton algorithm is based on successive two-dimensional Fourier transforms, significant speed-up can be achieved through the massive parallelization of dedicated compute graphics processing units (GPUs). We implemented the algorithm on a GPU, and found that individual holograms sufficient for our 512 by 512 pixel SLM could be calculated at a 50 Hz rate. Recently, Lee et al. demonstrated this approach to real-time, parallel transport of atoms trapped in optical tweezers [31].

Figure 9 shows an array of >500 foci created with a test setup. Here, the Fourier transforming lens had a focal length of 150 mm, so a large field of view could be achieved.

## 3.2. Control system

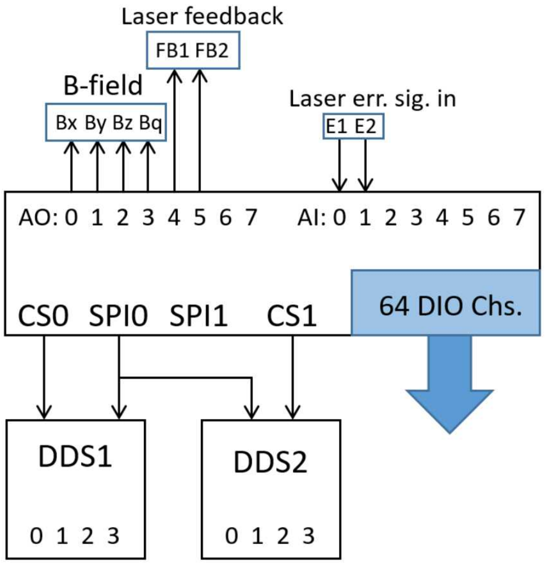

**Figure 10** FPGA analog and digital control lines. Analog out (AO) channels control magnetic field coils, and provide laser feedback control based on error signals read through the analog in (AI) channels. Digitial communication using the Serial Programming Interface (SPI) protocol controls the frequency, amplitdue and phase of eight independent direct digital synthesizer (DDS) channels. Additional digital input/output channels are available for switching other components, such as shuttering optical beams.

Our experimental control system is based on a field-programmable gate array (FPGA). Several factors motivated the choice of an FPGA for our control system: (1) Digital communication protocols, such as the commonly-used serial peripheral interface (SPI), are straightforward to implement natively on an FPGA, without need for additional board. (2) FPGAs can be integrated with numerous analog in (AI) and analog out (AO) lines, which open are useful for experimental control, including medium-bandwidth (10 kHz) feedback loops. (3) FPGA timing is hardware based, and can be synchronized with an input clock for 10 ns-scale timing resolution and high accuracy. (4) FPGAs are scalable, such that multiple FPGAs with similar or disparate functionality can be synchronized to easily increase control system functionality without increasing any computational overhead. (5) Logic executed on an FPGA runs natively in parallel, so adding additional functionality on the single-FPGA level will not affect how existing logic executes. (6) Timing and latency is deterministic and fixed, in contrast to software-based control systems.

Because the relevant entanglement dynamics of this system are expected to occur on the level of microseconds, the deterministic latency (e.g., no timing jitter), high-resolution timing, and scalable topology of FPGAs in particular motivated the choice of an FPGA-based control system. We utilized the National Instruments PXI-7853 "multifunction RIO" (RIO stands for reconfigurable input/output). Figure 10 shows the control system architecture based on the FPGA. The FPGA code is programmed with the LabVIEW software environment, and data can be passed through to, and read from, the host computer. We utilized a subset of the digital input/output (DIO) lines to create two SPI busses, of which a single bus was used to control two four channel direct digital synthesizers (DDSs) for a total of 8 frequency outputs, whose amplitude, phase, and frequency could be set on the 10 microsecond time scale per channel. The second SPI bus is unused, but could be activated in the FPGA code. Dedicated chip select (CS) lines determine which DDS board is actively receiving information over the SPI bus. In this way, many boards can be "daisy chained" onto a common SPI bus, and adding additional DDS channels is therefore simple. Analog outputs (AOs) control four magnetic coils used in the experiment, which will be described later. The lasers are locked via a digital feedback loop that uses two analog in (AI) channels to read the laser error signal, and two AO channels that tune the laser frequency to stay on resonance. A total of 64 extra DIO lines are left to switch logic-controlled components of the experiment. These lines are controllable via the FPGA directly or by host computer commands that are passed to the FPGA. In the latter case, timing is dictated by the host computer and by the communication between it and the FPGA, so any timing-critical sequences need to be pre-loaded onto the FPGA so they can be executed purely in hardware.

## 3.3. Laser systems

The laser system employed in this experiment all serve to trap and cool the atoms. The cooling laser for the magneto-optical trap (MOT) is an external cavity diode laser in the Littrow configuration, using the design of Ref. [49]. It is locked to the $F=4\rightarrow F'=3'\times 4'$ crossover transition of the Cesium $6\mathrm{S}_{1/2}\rightarrow 6\mathrm{P}_{3/2}$ transition, via saturated absorption frequency modulation (FM) spectroscopy. Feedback control of the laser frequency is achieved via a piezo-electric transducer that changes the grating angle within the Littrow cavity. The feedback loop transfer function is set by a digital feedback loop implemented in the control FPGA. Because the piezoelectric transducer is relatively slow, the loop bandwidth was limited to the few kHz range. The frequency modulation is added to the probe beam of the saturated absorption system by a 20 MHz resonant EOM; both the drive and demodulation are provided by two separate DDS channels, which allows digital tuning of the relative phase for optimal lock signal.

The repump laser, which serves to keep atoms out of the $F=3$ hyperfine manifold during the cooling cycle, is locked to the $F=3\rightarrow F'=3'\times 4'$ of the Cs $6\mathrm{S}_{1/2}\rightarrow 6\mathrm{P}_{3/2}$ transition. The lock error signal is also derived from FM spectroscopy in a saturated absorption setup, with details similar to those of the MOT cooling laser. However, unlike the cooling laser, the repump laser is a distributed feedback laser, with frequency tuning performed via current control. The feedback loop could operate with 100 kHz bandwidth, which seemed to be set by the latency of the FPGA AI and AO channels. It is possible that improvements to the FPGA code could lower the latency, and the bandwidth could be higher.

The third laser in the system is based on the same design as the MOT cooling laser, but operates at the magic wavelength of Cs of 935 nm[2]. The exact wavelength is not as important as is the case for lasers that are near-resonant Cs optical transitions, so this laser was left free-running. Based on our experience with the MOT laser of the same design, it could be expected to drift of order 100 MHz per day. The output of this laser goes through two stages of optical isolation before seeding a tapered amplifier for boosting the optical power from 20 mW to approximately 800 mW. The fiber-coupled output of the amplifier is sent to the experiment where it forms the optical tweezers.

In order to finely control the amplitude, power, and frequency of the cooling and repump lasers, as well as bring them onto resonance with the $F=4\rightarrow F'=5'$ and $F=3\rightarrow F'=4'$, respectively, we utilize acousto-optic modulators (AOMs). The AOM strategy is shown in Figure 11. Double-pass AOMs, centered at 110 MHz and with a total tuning bandwidth of 50 MHz per pass ( $\pm 25\ \mathrm{MHZ}$ about the central frequency), tune the laser frequency without strongly affecting the power. The final AOM in each path is set at a static frequency, but provides an additional shuttering mechanism for cooling and repump lasers. For the cooling laser, the double pass AOM is on-resonance at approximated 130 MHz, with is the upper range of the AOM bandwidth. This means that far red-detuned frequencies, important for polarization gradient cooling, can be achieved by tuning the AOM to its lower range of 90 MHz, which represents a total red detuning of 80 MHz in the double-pass configuration.

---

[2] We note that because of vector and tensor shifts of the $6\mathrm{P}_{3/2}$ state of Cs, the magic wavelength is polarization- and spin-dependent. We chose 935 nm as a compromise.

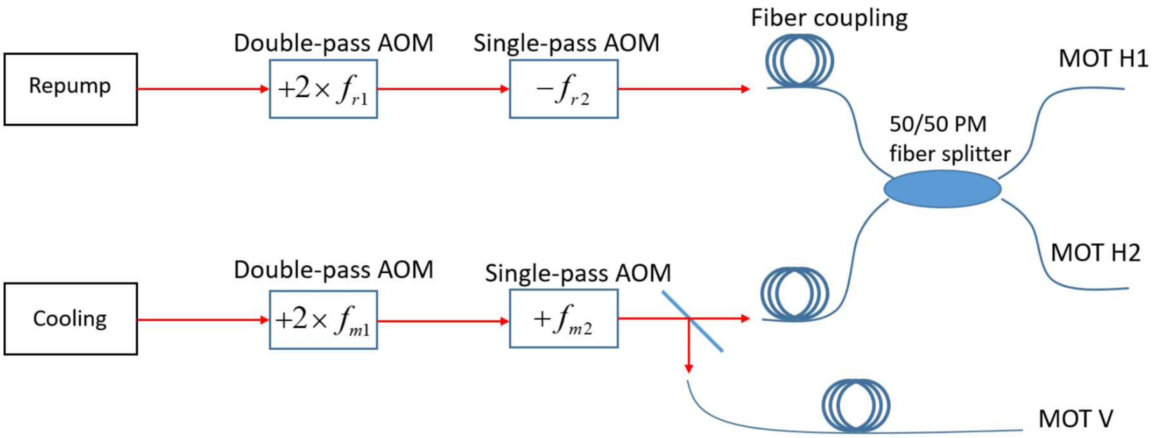

**Figure 11** Cooling and repump laser frequency shifting and delivery scheme. The cooling and repump light is shifted near resonance via a comination of double- and single-pass acousto-optic modulators (AOMs). The horizontal MOT beams are combined with rempump light with a 50/50 polarization-maintaining (PM) fiber beamsplitter. The relative power in the MOT vertical and horizontal beams is tunable with a half wave plate.

## 3.4. Vacuum system

The design of the vacuum system incorporated multiple design requirements. The most important requirement was that the vacuum was of sufficient quality that the lifetime of trapped atoms was at the 1 second scale, which requires background pressures in the $10^{-9}$ to $10^{-10}$ Torr range. Second, we needed optical access for all the planned beams: (1) MOT/repump beams, (2) optical tweezers, (3) Rydberg laser at 318 nm wavelength, and (4) other beams such as Raman beams and optical pumping on the D1 transition of Cs.

Because Borosilicate glasses have high absorption at UV wavelengths, we chose a science cell made from quartz glass. We chose to leave the glass without additional coating, as coating designs for both the near-IR and UV wavelengths in this experiment would be challenging (although possible).

In order to reduce the background pressure in the science cell, we added the option of a source MOT to our vacuum design. Although this source MOT was never used, it allows for the atomic dispenser to be removed from the science cell by a differential pumping tube. Consequently, the source cell also has a port for its own ion pump. Currently, the entire system is pumped by a single 20 L/s ion pump attached between the source chamber and science cell.

Figure 12 shows a picture of the vacuum assembly. The system is supported on a 1" thick stainless steel breadboard that is mounted on four 1.5" diameter posts that are filled with lead shot for improved vibration performance. An "upper mezzanine" provides optical access to the source chamber for future experiments. The vertical MOT beam is shared by the source and science chambers, and it traversed the vertical extent of the vacuum system. Three independent cesium metal dispensers are spot-welded to medium current feedthroughs in bother the source chamber and the six-way cube between the source and science chamber. When the dispensers closer to the science chamber are run in parallel, typical operating currents are between 1 and 2 amps for loading in the single-atom regime.

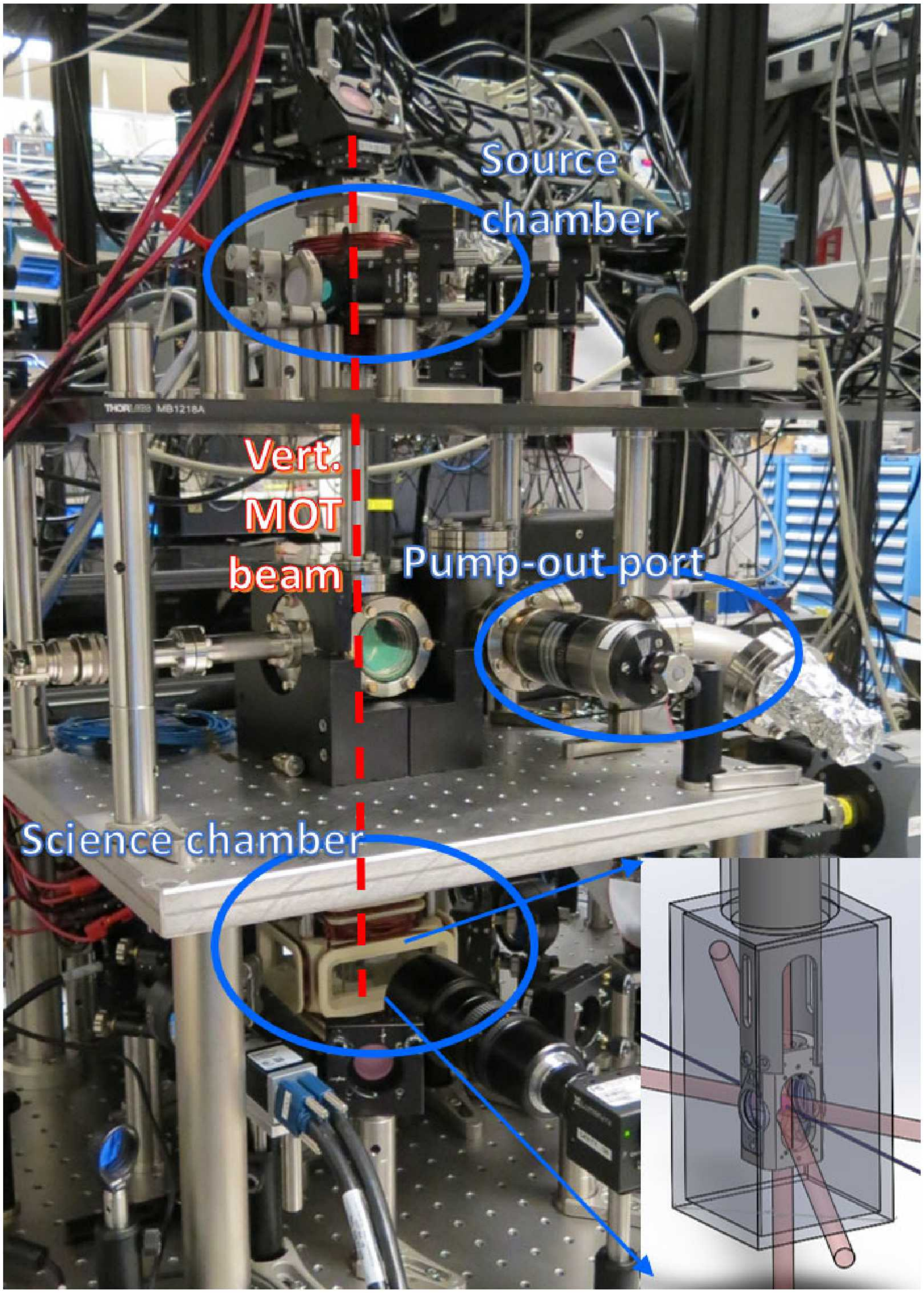

**Figure 12** Experimental chamber, including source chamber (top), support/pumping cube (middle), and science chamber (bottom). The source and middle chamber are separated by a low-conductivity differential pumping tube. The vertical MOT beam traverses the entire apparatus. Inset: drawing of the science chamber design with beam paths, shielding structure, and lens positioners shown.

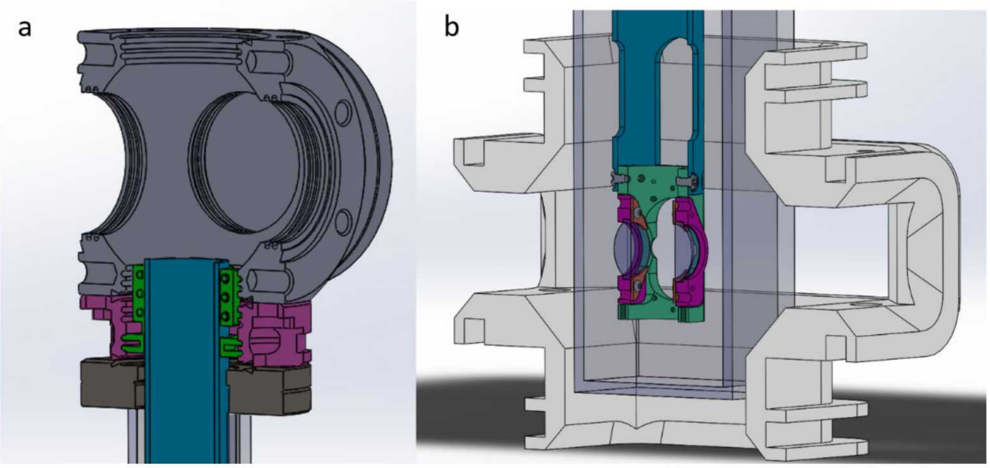

**Figure 13** Support strategy for shielding structure and lenses. (a) A stainless steel cylinder (blue) is rigidly clamped in the middle cube region via a “groove grabber” (green) that interfaces with a close coupler flange (purple). (b) the cylinder iterfaces with the shielding structure (light green), which supports the lens holder inserts (pink). The aspheric lenses are mechanically clamped in the lens holder inserts via a retaining jig (orange).

Because stray electric fields can shift Rydberg levels in a large and uncontrolled way, we designed a shielding structure for the interior of the science cell. The design of the internal structure is shown in Figure 13 and the inset of Figure 12. We designed a structure to precisely position the two in-vacuum lenses relative to each other, as well as provide optical access for the previously-enumerated beams. Additional information regarding the optical setup is given in the next section. Optional side and top panels, which were not installed for this work, provide additional shielding for electric fields as well as a mounting surface for electrodes, which were also not included at this stage of the project. To ensure cleanliness and low outgassing, the shielding structure and support tube were electro-polished. Figure 14 shows pictures of the shielding structure before the lenses were installed.

Because the objective lenses for the optical tweezer and atom imaging are also attached to the shielding structure, its stability is important. We chose to use a cylindrical tube to mount the shielding structure. The top part of the cylinder is clamped at the bottom flange of the six-way cube. In order to aid in assembly, the cylinder is clamped via a “groove grabber” assembly that is attached to a close coupler flange, as detailed in Figure 13a. A picture of the shield structure and its interface with the tube is shown in Figure 14.

Because a quadrupole magnetic field gradient defines the center of the MOT, and also because magnetic bias fields serve to define a quantization axis, we included 4 pairs of coils around the science cell, supported by the structure shown in Figure 13b. Three pairs of these coils were in the Helmholtz configuration to provide bias fields, while the fourth pair was in the anti-Helmholtz configuration for the quadrupole field. At 5 amps, the quadrupole coils should produce a gradient of roughly 15 G/cm at the center of the coil,

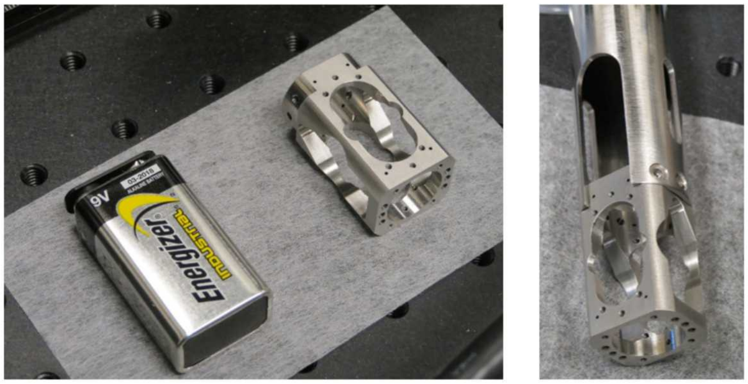

**Figure 14** Picture of the completed shielding structure, with familiar object for scale.

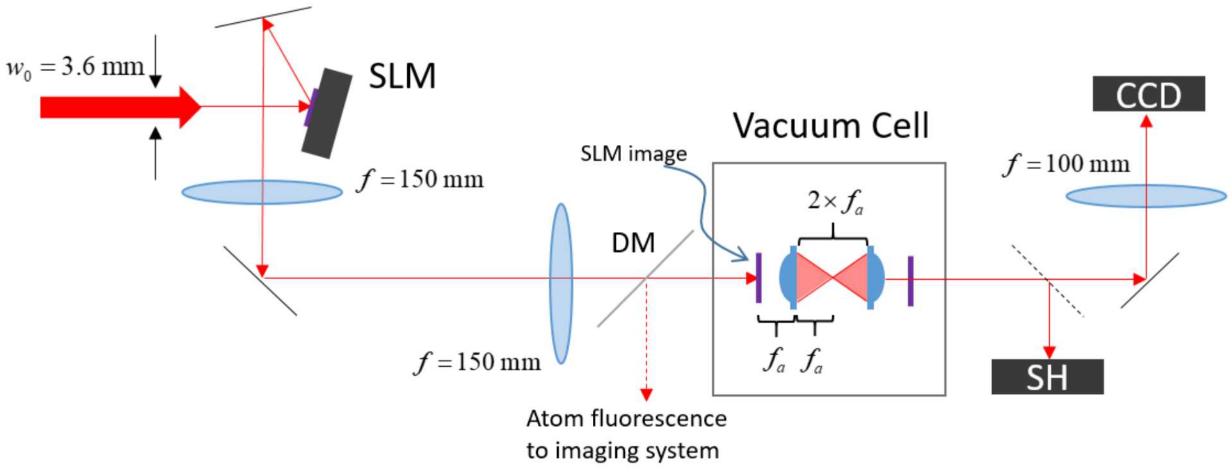

**Figure 15** Optical layout of the holographic trap generation system. A Gaussian beam with $1/e^2$ radius of 3.6 mm receives a phase imprint from the spatial light modulator (SLM). The image of the phase imprinted beam is relayed into the science cell with a $4f$ imaging system, where it is Fourier transformed by a high-NA asheric lens with effective focal length of $f_a = 10\text{ mm}$. An identical lens relays the input phase mask to the far side of the chamber, where it is anlyzed via wavefront analysis. An imaging system comprising the second high-NA lens and an imaging lens re-images the trap array onto a monitor camera (CCD) with a factor of 10 magnification.

in the direction perpendicular to the plane of both coils (i.e., the direction of strongest gradient). The other pairs of Helmholtz coils produce an approximate field of roughly 1 G/amp. All coils can run in steady-state at 5 amps. Any higher, and they begin to show signs of thermal runaway, and must be shut off. However, this does not preclude running at higher currents for short periods of time.

## 3.5. Imaging system

As discussed in the introduction, high-NA objective lenses enable wavelength-scale focal spot sizes for input fields that are comparable in extent to the lens input aperture. In the case of tweezer arrays created via digital holograms, Equation (10) also expresses the input/output scaling of the lens system, where the factor of $\lambda f$ converts the Fourier transform coordinates into real-space coordinates, which sets the scale factor for the optical tweezer array.

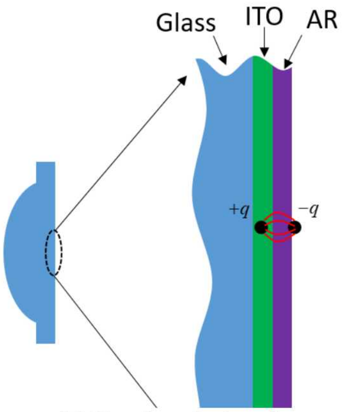

**Figure 16** Coating design for screening charges embedded in lens. An indium tin oxide layer is buried beneath the final anti-reflection coating

In order to create high quality optical traps, and for Equation (10) to exactly hold, we need to relay the image of the SLM to the Fourier plane of the high-NA lens. This approach was followed by Nogrette et al. [44], who point out that relaying the image also prevents vignetting in the optical system. Figure 15 shows the approach used to relay the Gaussian-illuminated SLM to the input focal plane of the high-NA aspheric lens. Multi-element lenses can provide good performance for high-NA applications, even at large working distances of >20 mm. However, high-NA imaging through a glass window, such as the vacuum chamber, causes spherical aberrations in the imaging system. One approach to simplifying such a system is to put the lens inside the vacuum chamber, which has been demonstrated with multi-

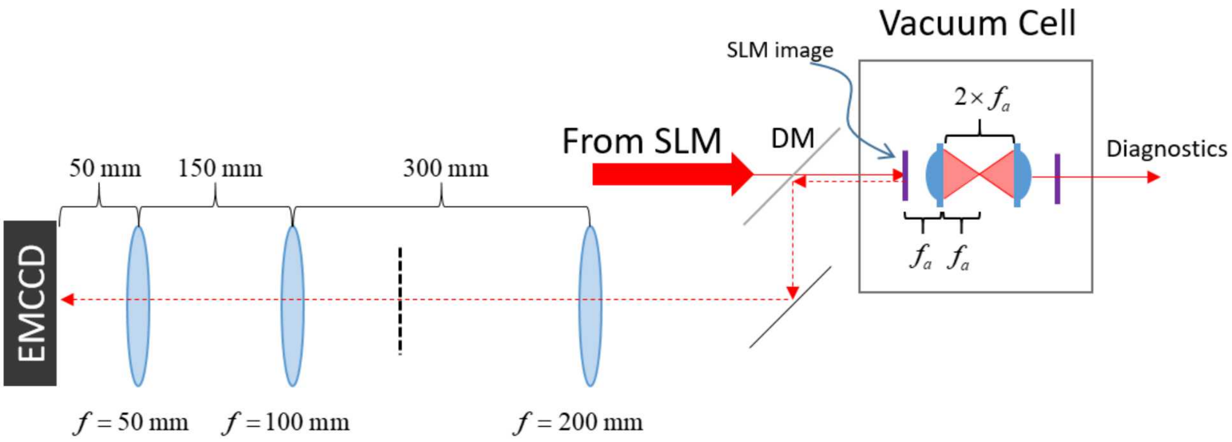

**Figure 17** Imaging system for detecting single atoms in optical tweezers. The dashed black line indicates an intermediate image plane, which is de-magnified by a factor of two onto the electron multiplying charge-coupled device (EMCCD) camera. With the high-NA lens effective focal length of 10 mm, the net magnification is a factor of 10. Therefore, each EMCCD pixel represents 800 nm in the trapping plane.

element objectives [17] and single-element aspheric lenses [50]. A custom aspheric lens for trapping Rubidium was developed by the Browaeys group at Institut d'Optique, with NA of 0.45 at 850 nm and working distance of 7 mm [51]. Because this lens is available commercially[3], and has good performance for our application, we chose it as our high-NA lens.

We installed a pair of high-NA lenses into the shielding structure. The lenses are held in precisely-machined mounts that interface with surfaces that maintain alignment of the two lenses at the level of 25 microns. Once in contact with the alignment surfaces, the mounts can still slide in the axial direction until they are locked in place with set screws. Before installing the pair of lenses into the vacuum chamber, we adjusted their relative alignment so that initially collimated trap light at 935 nm was re-collimated after passing through the pair of lenses. We used a Shack-Hartman wavefront sensor to measure residual quadratic phase factors on the transmitted wavefront for fine-tuning the alignment.

One challenge to overcome in Rydberg atom systems is the presence of a glass surface near the atoms. Because glass is an extremely good insulator, charges that are deposited, such as photo-electrons, tend to stay over long periods of time and can result in poorly controlled and time-varying electric fields, which strongly perturb the Rydberg energy levels [23]. One approach to circumvent this problem is to apply a conductive, transparent coating of indium tin oxide (ITO) coating to the lens surface, which serves to screen external charges and dissipate any charges that end up hitting the surface. However, the optical transmission of the lens can suffer, because a single ITO layer cannot be optimized over the same wavelength range that a multi-layer dielectric anti-reflection (AR) coating can. In order to improve the coating properties, we employed a different tactic. As shown in Figure 16, the ITO layer is between the lens and a final, optimized multilayer coating. We designed the coating such that there is an exposed annulus of ITO that makes contact with the electrically-grounded shield structure, and we have verified that the resistance between a point on the exposed annulus and the shield structure is low. Any charge that implants on the final AR coating layer will induce an opposite image charge, separated by less than a micron (the AR coating thickness). As a result, the electric field at the focal plan of the lens is reduced by a factor of $d_{\text{coat}} / f \simeq 10^{-4}$. This screening ratio compares favorably to the screening ratio of the open apertures of the shielding

---

[3] Lightpath Technologies lens code 355561.

structure, and therefore should not be a significant additional source of electric field noise. By measuring the transmission through a pair of lenses based on this design, we find that the transmission efficiency of a single lens at 935 nm is $\simeq 95\%$.

In addition to creating the array of optical tweezers, the high-NA lens also serves to collect fluorescence emitted by the atoms when they are driven by the MOT cooling light. This light is separated from the trapping light by a dichroic beam-splitter, and sent to an imaging system, shown in Figure 17, which has a total magnification factor of 10. The image is recorded on an electron multiplying charge coupled device (EMCCD) camera, with pixel size of 8 microns. The magnification factor of 10 is chosen to approximately match the magnified point spread function of single atoms to a single EMCCD pixel.

Finally, we note that the presence of a re-collimated trapping beam that is transmitted through the chamber is a powerful diagnostic tool [44]. We utilize a Shack-Hartmann wavefront sensor on the transmitted light to characterize the total wavefront aberration. We have developed a feedback loop to correct aberrations by applying corrections the SLM to flatten the transmitted wavefront, but this method was not implemented for the results presented here. We find that the transmitted wavefront does contain some significant aberrations, as shown in Figure 18, which will affect the trap quality. We expect that applying feedback to the SLM can correct the wavefront to have improved quality.

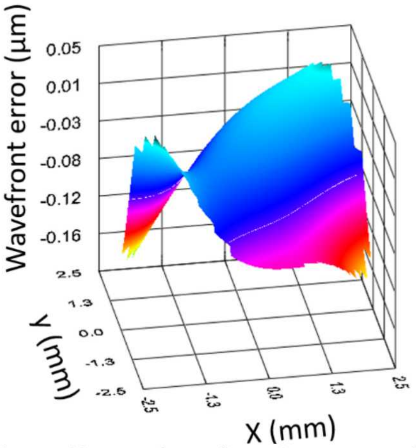

**Figure 18** Wavefront distortion measured by the Shack-Hartmann wavefront sensor on the far side of the chamber. The wavefront is flat to $\lambda/4$ over the region displayed here, which is approximately the $1/e$ (not $1/e^2$) diameter of the beam. The beam is not flat to $\lambda/4$ over its ± 3.5 mm $1/e^2$ extent, which indicates that correcting the aberrations with the SLM could yield improvements to the optical performance of the system.

# 4. OPTICAL TRAPPING RESULTS

In this section, we present initial results of trapping ultracold atoms in optical tweezers. We utilized the imaging system described in the previous section to produce the traps, image the trapped atoms, and characterize the trap quality.

## 4.1. Optical trap gallery

In this section, we display a variety of trapped atom patterns that demonstrate control over trap geometry. As a first case, we consider a 7 by 7 site square array. The phase pattern and re-imaged trap array are shown in Figure 21a, and Figure 21b, respectively. The diagnostic image is useful because it allows us to examine the quality of the traps when they are re-imaged outside the vacuum chamber. By fitting the width of a pair of traps, shown in Figure 19a, we find that the $1/e^2$ radius $w_0$ of the re-imaged traps is consistent with trap waists of 1.7 microns, which is approximate factor of two larger than we would expect, given the input waist of 3.6 mm.

We further analyze the width of the single atom point-spread function as imaged onto the EMCCD. We find that the width of the average intensity pattern of single trapped atoms, when characterized with a Gaussian fit function, has a $1/e^2$ radius of 1.7 microns Figure 19b. From diffraction theory, we expect the radius of the first Airy minimum to occur at 1.2 microns. Fitting an Airy function to the atomic point spread function yields 2.4 microns. In both cases, the fitting function matches the region of highest intensity, but fails to describe the data at larger distances (Figure 19b). We attribute this to aberrations in the system that need to be corrected. Further evidence of optical aberrations can be seen in the two-dimensional average images of trapped atoms, where "tails" are clearly visible in each imaged atom. These could be indicative of coma-type aberration. Our minimum resolvable trap separation was found to be 3 microns, a value consistent with the conclusion of these fits. Finally, we estimate that given our input power, measured beam waist, and approximate diffraction efficiency, the depth an individual trap in an array of total number of traps, $N_{\text{traps}}$, is approximately $50\text{ mK}/N_{\text{traps}}$. Considerable improvement can be made via improvements to the wavefront quality.

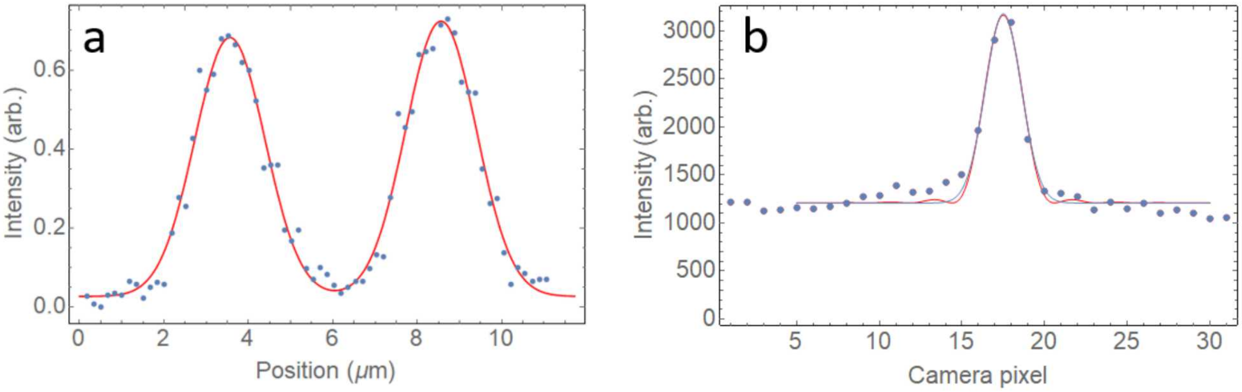

**Figure 19** Fit of a 1D segment of the intensity profile indicated in Figure 21b by the orange line. (a) We find that the width of the re-imaged traps corresponds to a $1/e^2$ intensity radius of $w_0 = 1.7\ \mu\text{m}$. (b) Fitting single-atom point-spread functions to both the Airy function and a Gaussian, which yield similar results for the central region. Each camera pixel represents 800 nm in the object plane, which contains the trapped atom. Neither functions fit the data well away from the intensity maximum, presumably because of the presence of aberrations in the imaging system. The Gaussian fit to the point spread function yields $w_0 = 1.7\ \mu\text{m}$, which matches the trap profile.

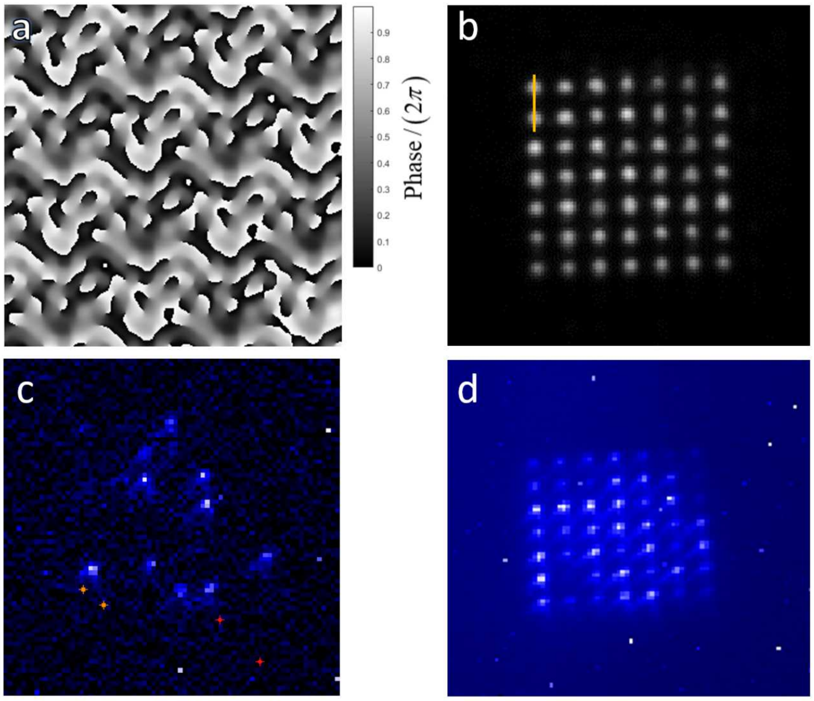

**Figure 21** 7 by 7 square lattice with 5 μm spacing between atoms and a total of 49 trap sites. (a) Computer generated hologram used to generate (b) the measured trapping potential. (c) Single shot of 100 ms averaging that shows a subset of the traps are loaded with single atoms. (d) Image of loaded traps averaged over many cycles.

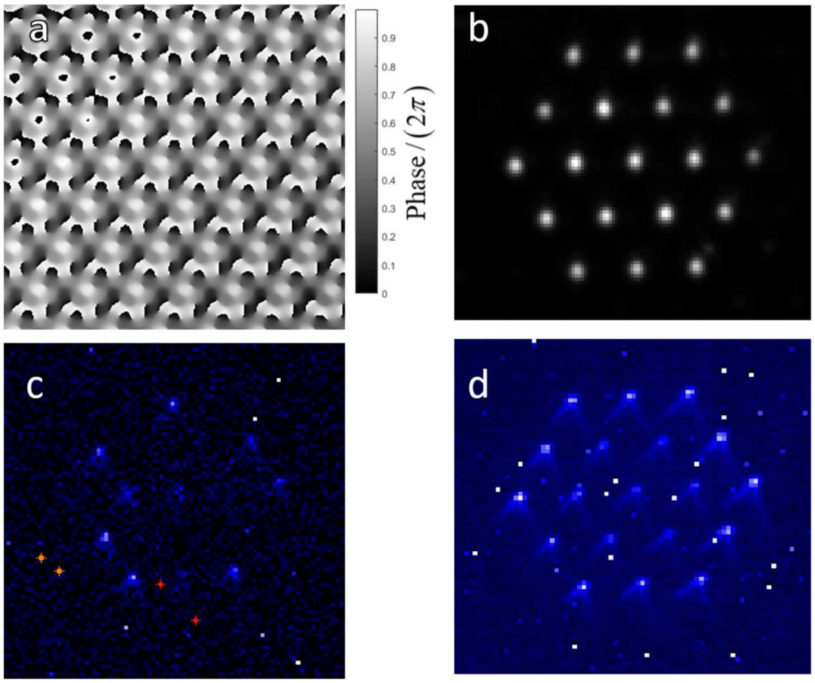

**Figure 20** Triangular lattice with 15 μm spacing between atoms and 19 trap sites. (a) Computer generated hologram used to generate (b) the measured trapping potential. (c) Single shot of 100 ms averaging that shows a subset of the traps are loaded with single atoms. (d) Image of loaded traps averaged over many cycles. "Tails" are clearly visible on the atom point spread function, indicating the presence of optical aberration, possibly coma.

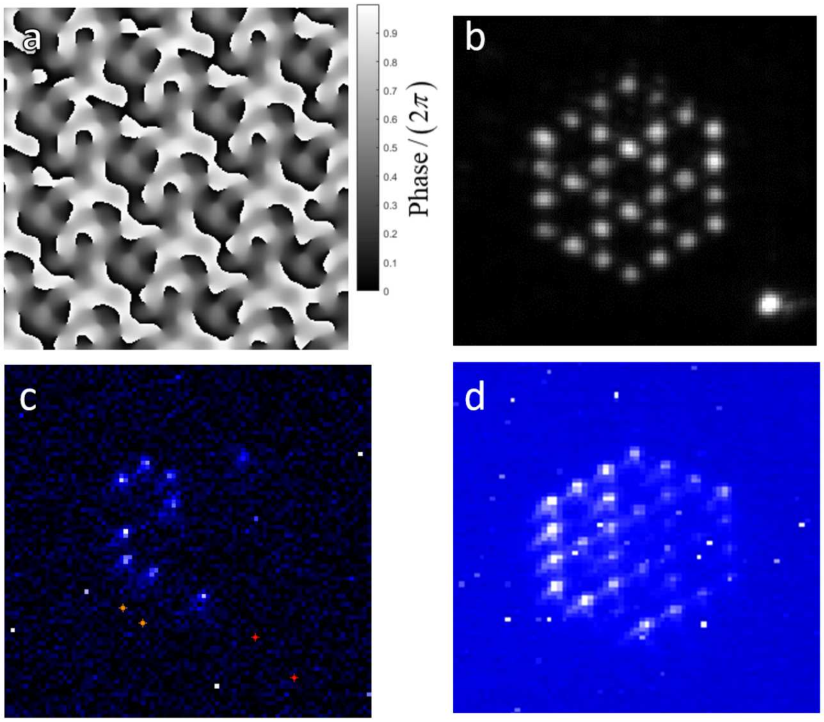

**Figure 23** Kagome lattice with 5 μm spacing between atoms and 30 trap sites. (a) Computer generated hologram used to generate (b) the measured trapping potential. (c) Single shot of 100 ms averaging that shows a subset of the traps are loaded with single atoms. (d) Image of loaded traps averaged over many cycles.

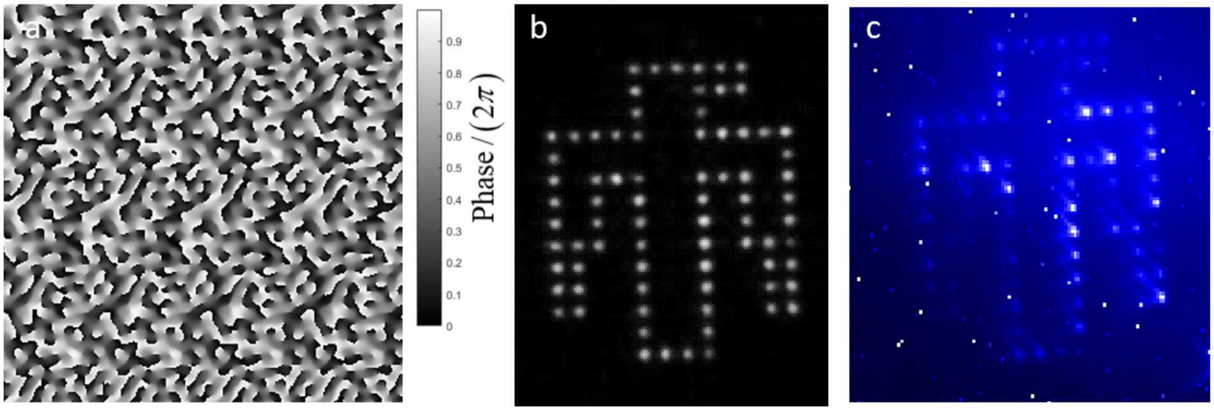

**Figure 22** Thunderbird logo trap configuration with 5 μm spacing between atoms and 76 trap sites. (a) Computer generated hologram used to generate (b) the measured trapping potential. (c) Image of loaded traps averaged over many cycles.

We also note that the width of the atomic distribution matches with the dipole trap profile. For sufficiently hot atoms, especially in shallow traps, the atom will explore a large region of the trap. It is possible that our point spread function is limited by this effect, and further characterization of the point spread function under different conditions, such as deeper traps, could help determine if this effect is important in our imaging system characterization.

Figure 19, Figure 21, and Figure 20 show three types of trapping configurations that can be of interest: the square lattice, the Kagome lattice, and the triangular lattice. In the first two configurations, the minimum atom spacing is 5 microns, which in the triangular lattice, the atom spacing is 15 microns, representing a field of view of 60 microns.

We conclude this section with a trap arrangement that is not of practical interest, but underscores the flexibility of this approach for creating arbitrary configurations. Figure 22 shows the Sandia Thunderbird logo, and the resulting trap loading. Because of the large number of traps, the loading efficiency is poor.

## 4.2. Time-domain signal

In any operation involving a Rydberg atom or a hyperfine ground state, a typical final step is state detection. Excitation to Rydberg levels is typically identified via the presence of loss (e.g., an atom is not trappable because it has been excited to the Rydberg manifold and leaves the system). In order to check the detection efficiency of this system, we analyzed the time-dependent fluorescence signal from the optical traps. While we implemented a scheme to detect atoms in parallel, we focus here on an individual site. Using a ring configuration with a total of 20 atoms, with 4.7 micron spacing between atoms, we integrated the EMCCD signal in a region of interested that was centered on one atom, as shown in Figure 24a. With an integration time of 100 ms, the "telegraphic" signature of single-atom loading was apparent. When we made a histogram of the data, shown in a clear separation between zero and one atoms is observed. This level of separation is sufficient for state detection with $> 99.5\%$ reliability. We note that the probability of loading a single atom is below 50%, with a loading probability of 15%. We hypothesize that this low loading rate is a result of the relatively large trap volume, which reduces the effectiveness of the collisional blockade. To stay in the single atom loading regime, the loading rate must therefore be kept low, which leads to less than 50% average trap occupancy. Taking this measurement with deeper traps (by increasing power or reducing the number of traps) could help to clarify the cause of this observation.

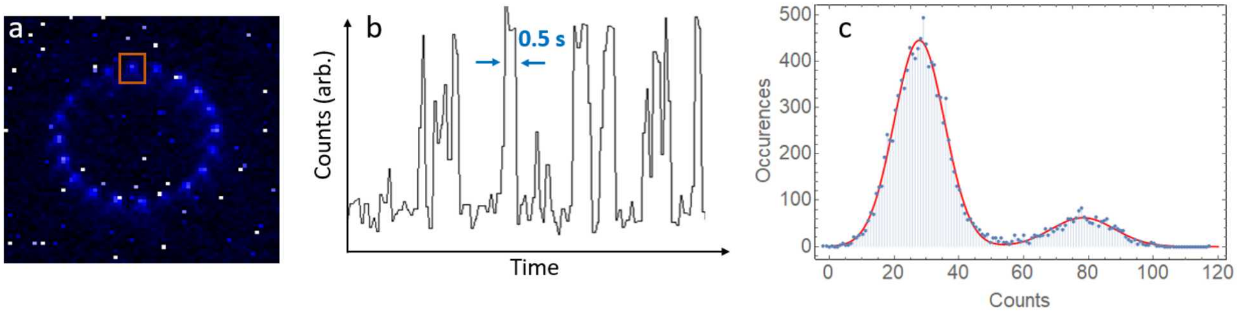

**Figure 24** (a) Ring trap array with 20 atoms and 30 µm diameter. This image is averaged over many exposures (b) Time domain signal of EMCCD pixel counts in the region of interest indicated by the orange box in (a). Here, the integration time was 100 ms. While actively loading with the MOT, atoms stayed trapped for typical durations of 500 ms. (c) Histogram of count values in 100 ms integration time bins. The presence or absence of an atom in this specific trap site is clearly resolved.

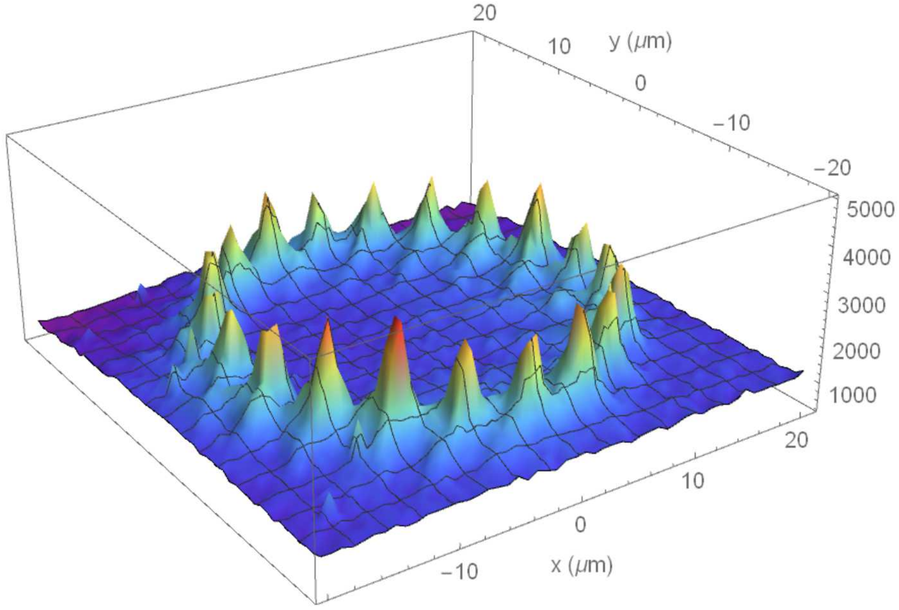

**Figure 25** Three-dimensional view of atoms in the ring tap. The single atoms are clearly resolved, with 4.7 micron separation.

## 5. CONCLUSION

Controlled many-body quantum systems will impact fundamental science, technology, and our understanding of complex quantum systems found in nature. Key attributes for any laboratory testbed will be control of interactions and connectivity; and individual atom detection and control. The approach presented here lays the groundwork for creating such a system from the ground up, atom by atom, in a highly scalable platform.

When combined with the single-photon Rydberg excitation laser, Ising models can be implemented in this system [27], and have recently been demonstrated by several groups [37, 38, 24]. By control of the excitation field, adiabatic sweeps prepare crystallized states, which can be converted to the maximally entangled GHZ state. We foresee that the method of using geometric frustration for entanglement will be a robust tool for creating large-scale entanglement, with the possibility of creating highly-entangled states in small volumes. Other opportunities for this system will be studies of quantum annealing for applications in optimization problems, and parallel studies of pair-wise entangling gates.

# REFERENCES

[1] L. I. R. Gil, R. Mukherjee, E. M. Bridge, M. P. A. Jones and T. Pohl, "Spin Squeezing in a Rydberg Lattice Clock," *Phys. Rev. Lett.,* vol. 112, p. 103601, 2014.

[2] T. Keating, C. H. Baldwin, Y.-Y. Jau, J. Lee, G. W. Biedermann and I. H. Deutsch, "Arbitrary Dicke-State Control of Symmetric Rydberg Ensembles," *Phys. Rev. Lett.,* vol. 117, p. 213601, 2016.

[3] M. H. Devorer and R. J. Schoelkopf, "Superconducting circuits for quantum information: An outlook," *Science,* vol. 339, p. 1169–1174, 2013.

[4] D. D. Awschalom, L. C. Basset, A. S. Dzurak, E. L. Hu and J. R. Petta, "Quantum spintronics: Engineering and manipulating atom-like spins in semiconductors.," *Science,* vol. 339, pp. 1174-1179, 2013.

[5] R. Barends, J. Kelly, A. Megrant, A. Veitia, D. Sank, E. Jeffrey, T. C. White, J. Mutus, A. G. Fowler, B. Campbell, Y. Chen, Z. Chen, B. Chiaro, A. Dunsworth, C. Neill, P. O'Malley, P. Roushan, A. Vainsencher, J. Wenner, A. N. Korotkov, A. N. Cleland and J. M. Martinis, "Superconducting quantum circuits at the surface code threshold for fault tolerance," *Nature,* vol. 508, p. 500–503, 2014.

[6] J. L. F. A. &. V. J. O'Brien, "Photonic quantum technologies," *Nature Photon.,* vol. 3, p. 687–695, 2009.

[7] K. R. Brown, A. C. Wilson, Y. Colombe, C. Ospelkaus, A. M. Meier, E. Knill, D. Leibfried and D. J. Wineland, "Single-qubit-gate error below 10−4 in a trapped ion," *Phys. Rev. A,* vol. 84, p. 030303, 2011.

[8] C. Monroe and J. Kim, "Scaling the ion trap quantum processor," *Science,* vol. 339, p. 1164–1169, 2013.

[9] D. Nigg, M. Muller, E. A. Martinez, P. Schindler, M. Hennrich, T. Monz, M. A. Martin-Delgado and R. Blatt, "Quantum computations on a topologically encoded qubit," *Science,* vol. 345, pp. 302-305, 2014.

[10] K. D. L. X. &. W. D. S. Nelson, "Imaging single atoms in a three-dimensional array," *Nature Phys.,* vol. 3, p. 556–560, 2007.

[11] T. Wilk, A. Gaetan, C. Evellin, J. Wolters, Y. Miroshnychenko, P. Grangier and A. Browaeys, "Entanglement of Two Individual Neutral Atoms Using Rydberg Blockade," *Phys. Rev. Lett.,* vol. 104, p. 010502, 2010.

[12] X. L. Zhang, L. Isenhower, A. T. Gill, T. G. Walker and M. Saffman, "Deterministic entanglement of two neutral atoms via Rydberg blockade," *Phys. Rev. A,* vol. 82, p. 030306(R), 2010.

[13] D. Barredo, S. de Leseleuc, V. Lienhard, T. Lahaye and A. Browaeys, "An atom-by-atom assembler of defect-free arbitrary two-dimensional atomic arrays," *Science,* vol. 354, pp. 1021-1023, 2016.

[14] D. Barredo, V. Lienhard, S. de Leseleuc, T. Lahaye and A. Browaeys, "Synthetic three-dimensional atomic structures assembled atom by atom," *Nature,* vol. 561, pp. 79-82, 2018.

[15] C. L. Degen, F. Reinhard and P. Cappellaro, "Quantum sensing," *Rev. Mod. Phys.,* vol. 89, p. 035002, 2017.

[16] I. Bloch, J. Dalibar and S. Nascimbene, "Quantum simulations with ultracold quantum gases," *Nature Phys.,* vol. 8, p. pages 267–276, 2012.

[17] G. R. I. P. P. G. N. Schlosser, "Sub-poissonian loading of single atoms in a microscopic dipole trap," *Nature,* vol. 411, p. pages 1024–1027, 2001.

[18] A. M. Kaufman, B. J. Lester and C. A. Regal, "Cooling a Single Atom in an Optical Tweezer to Its Quantum Ground State," *Phys. Rev. X,* vol. 2, p. 041014, 2012.

[19] A. Mazurenko, C. S. Chiu, G. Ji, M. F. Parson, M. Kanasz-Nagy, R. Schmidt, F. Grusdt, E. Demler, D. Greif and M. Greiner, "A cold-atom Fermi–Hubbard antiferromagnet," *Nature,* vol. 545, pp. 462-466, 2017.

[20] M. Greiner, O. Mandel, T. Esslinger, T. W. Hansch and I. Bloch, "Quantum phase transition from a superfluid to a Mott insulator in a gas of ultracold atoms," *Nature,* vol. 415, pp. 39-44, 2002.

[21] S. Trotzky, P. Cheinet, S. Folling, M. Feld, U. Schnorrberger, A. M. Rey, A. Polkovnikov, E. A. Demler, M. D. Lukin and I. Bloch, "Time-Resolved Observation and Control of Superexchange Interactions with Ultracold Atoms in Optical Lattices," *Science,* vol. 319, no. 5861, pp. 295-299, 2008.

[22] A. W. Glaetzle, M. Dalmonte, R. Nath, C. Gross, I. Bloch and P. Zoller, "Designing Frustrated Quantum Magnets with Laser-Dressed Rydberg Atoms," *Phys. Rev. Lett.,* vol. 114, p. 173002, 2015.

[23] S. A. Moses, J. P. Covey, M. T. Miecnikowski, B. Yan, B. Gadway, J. Ye and D. S. Jin, "Creation of a low-entropy quantum gas of polar molecules in an optical lattice," *Science,* vol. 350, no. 6261, pp. 659-662, 2015.

[24] J. W. Britton, B. C. Sawyer, A. C. Keith, C.-C. J. Wang, J. K. Freericks, H. Uys, M. J. Biercuk and J. J. Bollinger, "Engineered two-dimensional Ising interactions in a trapped-ion quantum simulator with hundredes of spins," *Nature,* vol. 484, pp. 489-492, 2012.

[25] H. Labuhn, D. Barredo, S. Ravets, S. de Leseleuc, T. Macri, T. Lahaye and A. Browaeys, "Tunable two-dimensional arrays of single Rydberg atoms for realizing quantum Ising models," *Nature,* vol. 534, pp. 667-670, 2016.

[26] D. Jaksch, J. I. Cirac, P. Zoller, S. L. Rolston, R. Cote and M. D. Lukin, "Fast Quantum Gates for Neutral Atoms," *Phys. Rev. Lett.,* vol. 85, pp. 2208-2211, 2000.

[27] M. Saffman, T. G. Walker, K. Molmer and , "Quantum information with Rydberg atoms," *Rev. Mod. Phys.,* vol. 82, p. 2313, 2010.

[28] A. Hankin, Y.-Y. Jau, L. P. Parazzoli, C. W. Chou, D. J. Armstrong, A. J. Landahl and G. W. Biedermann, "Two-atom Rydberg blockade using direct 6S to nP excitation," *Phys. Rev. A,* vol. 89, p. 033416, 2014.

[29] H. Bernien, S. Schwartz, A. Keesling, H. Levine, A. Omran, H. Pichler, S. Choi, A. S. Zibrob, M. Endres, M. Greiner, V. Vuletic and M. D. Lukin, "Probing many-body dynamics on a 51-atom quantum simulator," *Nature,* vol. 551, pp. 579-584, 2017.

[30] T. Pohl, E. Demler and M. D. Lukin, "Dynamical Crystallization in the Dipole Blockade of Ultracold Atoms," *Phys. Rev. Lett.,* p. 043002, 2010.

[31] M. Khazali, H. W. Lau, A. Humeniuk and C. Simon, "Large energy superpositions via Rydberg dressing," *Phys. Rev. A,* vol. 94, p. 023408, 2016.

[32] P. Schauss, "Quantum simulation of transverse Ising models with Rydberg atoms," *Quantum Sci. Technol.,* vol. 3, p. 023001, 2018.

[33] M. W. Y. B. R. Grimm, "Optical Dipole Traps for Neutral Atoms," *Adv. In Atom. Mol. and Opt. Phys.,* vol. 42, pp. 95-170, 2000.

[34] A. Hankin, "Rydberg Excitation of Single Atoms for Applications in Quantum Information and Metrology," *PhD Thesis,* 2015.

[35] M. Endres, H. Bernien, A. Keesling, H. Levine and E. R. Anschuetz, "Atom-by-atom assembly of defect-free one-dimensional cold atom arrays," *Science,* vol. 354, pp. 1024-1027, 2016.

[36] W. Lee, H. Kim and J. Ahn, "Defect-free atomic array formation using the Hungarian matching algorithm," *Phys. Rev. A,* vol. 95, p. 053424, 2017.

[37] J. Honer, H. Weimer, T. Pfau and H. P. Buchler, "Collective Many-Body Interaction in Rydberg Dressed Atoms," *Phys. Rev. Lett.,* vol. 105, p. 160404, 2010.

[38] Y.-Y. Jau, A. M. Hankin, T. Keatin, I. H. Deutsch and G. W. Biedermann, "Entangling atomic spins with a Rydberg-dressed spin-flip blockade," *Nat. Phys.,* vol. 12, pp. 71-74, 2016.

[39] T. Keating, R. L. Cook, A. M. Hankin, Y.-Y. Jau, G. W. Biedermann and I. H. Deutsch, "Robust quantum logic in neutral atoms via adiabatic Rydberg dressing," *Phys. Rev. A,* vol. 91, p. 012337, 2015.

[40] G. Biedermann, "A new approach to entangling neutral atoms," *SAND2016-11861,* 2016.

[41] e. a. A. M. Hankin, "Two-atom Rydberg blockade using direct 6S to nP excitation," *Phys. Rev. A,* vol. 89, p. 033416 , 2014.

[42] H. Kim, Y. Park, K. Kim, H.-S. Sim and J. Ahn, "Detailed Balance of Thermalization Dynamics in Rydberg-Atom Quantum Simulators," *Phys. Rev. Lett.,* vol. 120, p. 180502, 2018.

[43] J. Lee, M. J. Martin, Y.-Y. Jau, T. Keating, I. H. Deutsch and G. W. Biedermann, "Demonstration of the Jaynes-Cummings ladder with Rydberg-dressed atoms," *Phys. Rev. A,* vol. 95, p. 041801(R), 2016.

[44] M. K. a. M. Ueda, "Squeezed spin states," *Phys. Rev. A,* vol. 47, pp. 5138-5143, 1993.

[45] C. A. e. a. Sackett, C. A. Sackett, D. Kielpinski, B. E. King, C. Langer, V. Meyer, C. J. Myatt, M. Rowe, Q. A. Turchette, W. M. Itano, D. J. Wineland and C. Monroe, "Experimental entanglement of four particles," *Nature,* vol. 404, pp. 256-259, 2000.

[46] M. J. M. G. W. Biedermann, "CPHASE gate with Rydberg atoms (CPHAR)," *SAND2017-12802,* 2018.

[47] S. Bergamini, B. Darquie, M. Jones, L. Jacubowiez, A. Browaeys and P. Grangier, "Holographic generation of microtrap arrays for single atoms by use of a programmable phase modulator," *J. Optical Soc. Am. B,* vol. 21, no. 11, pp. 1889-1894, 2004.

[48] F. Nogrette, H. Labuhn, S. Ravets, D. Barredo, L. Beguin, A. Vernier, T. Lahaye and A. Browaeys, "Single-Atom Trapping in Holographic 2D Arrays of Microtraps with Arbitrary Geometries," *Phys. Rev. X,* vol. 4, p. 021034, 2014.

[49] H. Kim, W. Lee, H.-G. Lee, H. Jo, Y. Song and J. Ahn, "In situ single-atom array synthesis using dynamic holographic optical tweezers," *Nat. Comm.,* vol. 7, p. 13317, 2016.

[50] W. Lee, H. Kim and J. Ahn, "Three-dimensional rearrangement of single atoms using actively controlled optical microtraps," *Optics Express,* vol. 24, no. 9, pp. 9816-9825, 2016.

[51] J. W. Goodman, Fourier Optics, Greenwood Village: Roberts and Company Publishers, 2005.

[52] R. W. Gerchberg and W. O. Saxton, "A practical algorithm for the determination of the phase from image and diffraction plane pictures," *Optik,* vol. 35, p. 237, 1972.

[53] E. C. Cook, P. J. Martin, T. L. Brown-Heft, J. C. Garman and D. A. Steck, "High passive-stability diode-laser design for use in atomic-physics experiments".

[54] e. a. Y. R. P. Sortais, "Diffraction-limited optics for single-atom manipulation," *Phys. Rev. A,* vol. 75, p. 013406 , 2007.

[55] L. Beguin, "Measurement of the van der Waals interaction between," *PhD Thesis,* 2013.

# DISTRIBUTION

### Hardcopy—External

| Number of Copies | Name | Company Name and Company Mailing Address |
|---|---|---|
| | | |
| | | |

### Hardcopy—Internal

| Number of Copies | Name | Org. | Mailstop |
|---|---|---|---|
| | | | |
| | | | |

### Email—External [redacted]

| Name | Company Email Address | Company Name |
|---|---|---|
| | | |
| | | |

### Email—Internal

| Name | Org. | Sandia Email Address |
|---|---|---|
| | | |
| | | |
| | | |
| | | |
| Technical Library | 9536 | libref@sandia.gov |

This page left blank

This page left blank